Science Advances

Supplementary Materials for

The physics of cement cohesion

Abhay Goya*, Ivan Palaia, Katerina Ioannidou, Franz-Josef Ulm, Henri van Damme,
Roland J.-M. Pellenq, Emmanuel Trizac, Emanuela Del Gado*

*Corresponding author. Email: ag1473@georgetown.edu (A.G.); ed610@georgetown.edu (E.D.G.)

This PDF file includes:

S1 Ion and water dynamics

In this section, we expand on the dynamics data shown in Figs. 3b and 4d. The plots in the main paper showed data for a single $q = q_z$ value, picked to show the trends in dynamics with σ and D, and here we include the data for all q values for the different σ and D considered (with evenly spaced values of q ranging from $q = 2\pi/D$ to $q = 10\,\text{Å}^{-1}$). We also take this opportunity to explain in more detail the comparisons with experimental measurements.

At large separations, most of the water is not associated with ions. For water that is bound in hydration shells at time $t = 0$ (plotted in Fig. S1a), we observe a complete decay in correlations over the simulation–albeit at a slightly slower rate than with the free water (Fig. S1b). While energetically favorable, Calcium hydration shells are highly dynamic with residence times $t_{res} \simeq 7 \cdot 10^5$ fs [38], and we observe significant decay in $F_s(q_z, t)$, even for bound water, indicating that the water can move back and forth between free and bound states and does not stay closely attached to the ions, which are instead clearly localized. In confinement, the ions become highly localized in the z direction, as demonstrated by plateaus in $F_s(q_z, t)$ (Fig. S1c). Due to the formation of hydration shells and geometric/packing constraints in confinement, this localization extends to the water, as seen by the relatively slow decays in Fig. S1d (quite slower when compared to the dynamics shown in Fig. S1b). Water-ion bond lifetimes measured from bond correlations are found on the order of $O(10^5\text{fs})$, indicating that correlations in water dynamics should still decrease faster then for ions, as we indeed observe. In addition, we find that for specific q values ($4\pi/D$, $8\pi/D$) the correlations exhibit a larger decrease, suggesting that these length scales correspond to specific distances at which elementary rearrangements of the water molecules can occur in confinement.

Upon increasing surface charge to $\sigma = 3e^-/\text{nm}^2$, which would correspond to the end of hydration, we discover a drastic change in the dynamics. $F_s(q_z, t)$ for the ions (plotted in Fig. S2a) exhibits even stronger localization with very high plateaus in the correlation. As this effect persists at $q = 10\,\text{Å}^{-1}$, this localization holds for length scales smaller than an angstrom, and we infer that this signal corresponds to the localization of the ions near the surfaces, consistent with the density profiles averaged over time shown in Fig. 2. The plot shown is for a separation of $D = 10\,\text{Å}$, but $F_s(q_z, t)$ for the ions is very similar up to $D = 40\,\text{Å}$—the highest separation simulated.

Starting at low separation (Fig. S2b), we see that the water behavior closely follows the ion dynamics. The correlations drops offto a lower valued plateau, meaning the localization is not quite as strong as for the ions, but it is clearly there for the water as well. The oscillations in Fig. S2b also mirror those exhibited by the ions, showing how strongly the water dynamics are coupled to those of the ions. These strong and long-lasting dynamical correlations are evidence of the formation of strongly correlated ion-water assemblies. While similar structures are observed at lower surface charges, the residence time of water molecules in the hydration shells is much lower, and thus the water correlations are not as long-lived. Instead, at high σ, the ion-water assemblies persist through the simulation time and the bound water remains highly localized even for $t > 10^5$ fs.

The same picture persists even at larger separations (Fig. S2c). However, while at lower separations most of the water is bound to ions, at $D = 40\,\text{Å}$ we observe drastically different behavior for bound and free water. The bound water, i.e. the water in the ion hydration shells, behaves exactly the same at $D = 40\,\text{Å}$ as at $D = 10\,\text{Å}$. This water is strongly coupled to the ions and they move (or rather do not move) in unison. Instead, the dynamics of free water (Fig. S2d) is substantially uncorrelated from the ions. This "free" water is, of course, still confined by the C-S-H walls and exhibits relaxation times comparable to those measured via experiments on water in cement pores [63]. However, the fact that there is no localization in the free water, indicates that the dynamical behavior of the bound water is largely determined by electrostatic interactions with ions and thermodynamics of n-mers rather than the confinement effects.

This clear separation of dynamics has been documented extensively in experiments on hydrating cement. Quasi-elastic neutron scattering (QENS) and nuclear magnetic resonance (NMR) experiments demonstrate that, as hydration
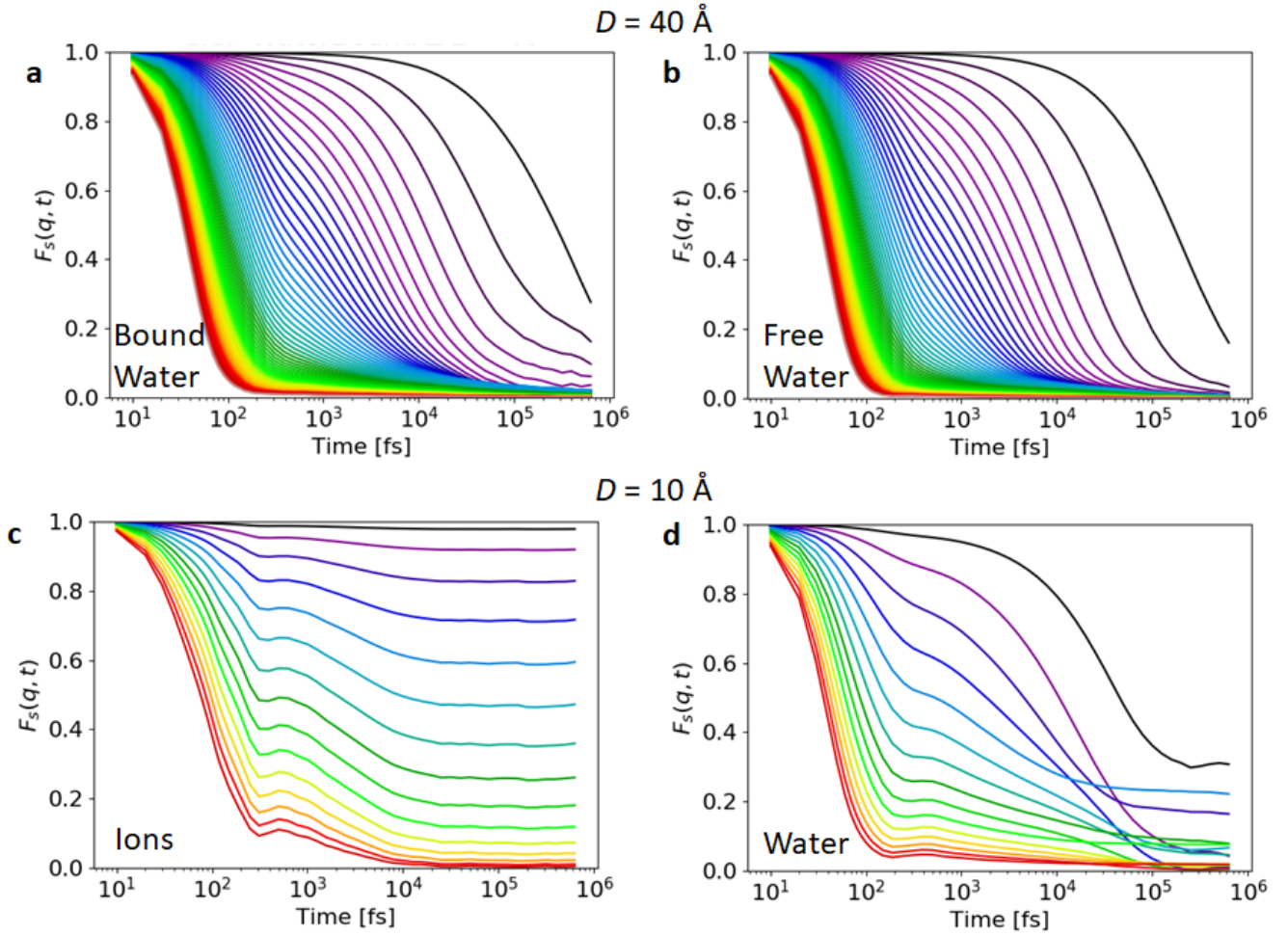
FIG. S1. Self intermediate scattering function at $\sigma = 1e^-/\mathrm{nm}^2$ in the z direction (normal to surface plane), for ions or water. Color indicates q from $q = 2\pi/D$ for black to $q = 10\,\text{Å}^{-1}$ for red. Results for bound (a) and free (b) water at $D = 40\,\text{Å}$, classified by whether they are bound to an ion at $t = 0$, exhibit significant decays in correlation over simulation times: though slightly slower for bound water than free water. The water dynamics diverge from that of the ions due to the finite ion-water bond lifetime. However, upon increasing confinement, the situation changes. Ions (c) at $D = 10\,\text{Å}$ exhibit plateaus due to the formation of layers and limited mobility. This partially extends to the water (d) which exhibits much slower decays compared to the water at $D = 40\,\text{Å}$ (ion correlations are relatively unaffected by changes in D). Additionally, we find that for specific q values ($4\pi/D$, $8\pi/D$) the correlations exhibit a larger decrease, suggesting that these length scales correspond to specific distances at which elementary rearrangements of the water molecules can occur in confinement. Note that such q-dependent features are erased at larger separations where water mobility is less limited.

progresses and C-S-H stoichiometry evolves while it progressively aggregates into a porous structure, an increasing fraction of water becomes significantly slower and is considered as physically bound [25–27]. Hence in hydrating cement there exist three populations of water: chemically bound, constrained (i.e. physically bound), and unbound. While our model does not resolve the chemically bound water, the characterization we provide of the "bound" and "free" water is, in fact, in good agreement with the QENS and NMR experimental characterization of constrained and unbound water. The intermediate scattering functions we compute are, in fact, directly related to the time correlations of the scattering intensity measured in QENS experiments (with the caveat that here we are computing the signal from the incoherent scattering, but the same signature would be seen in the coherent one).

Not only do our data confirm the experimental observations on the physically bound water, but they also provide the insight that such water is the one corresponding to the hydrated (or partially hydrated) ions, which constitute our ion-water interlocked structures. Our simulations show that this effect is dependent on the surface charge density σ, and at low σ the water bound to ions is dynamically similar to the free water (Fig. S1). Additionally, at fixed σ, an increase in confinement also raises the fraction of bound water (Fig. 4e). Both effects are consistent with the
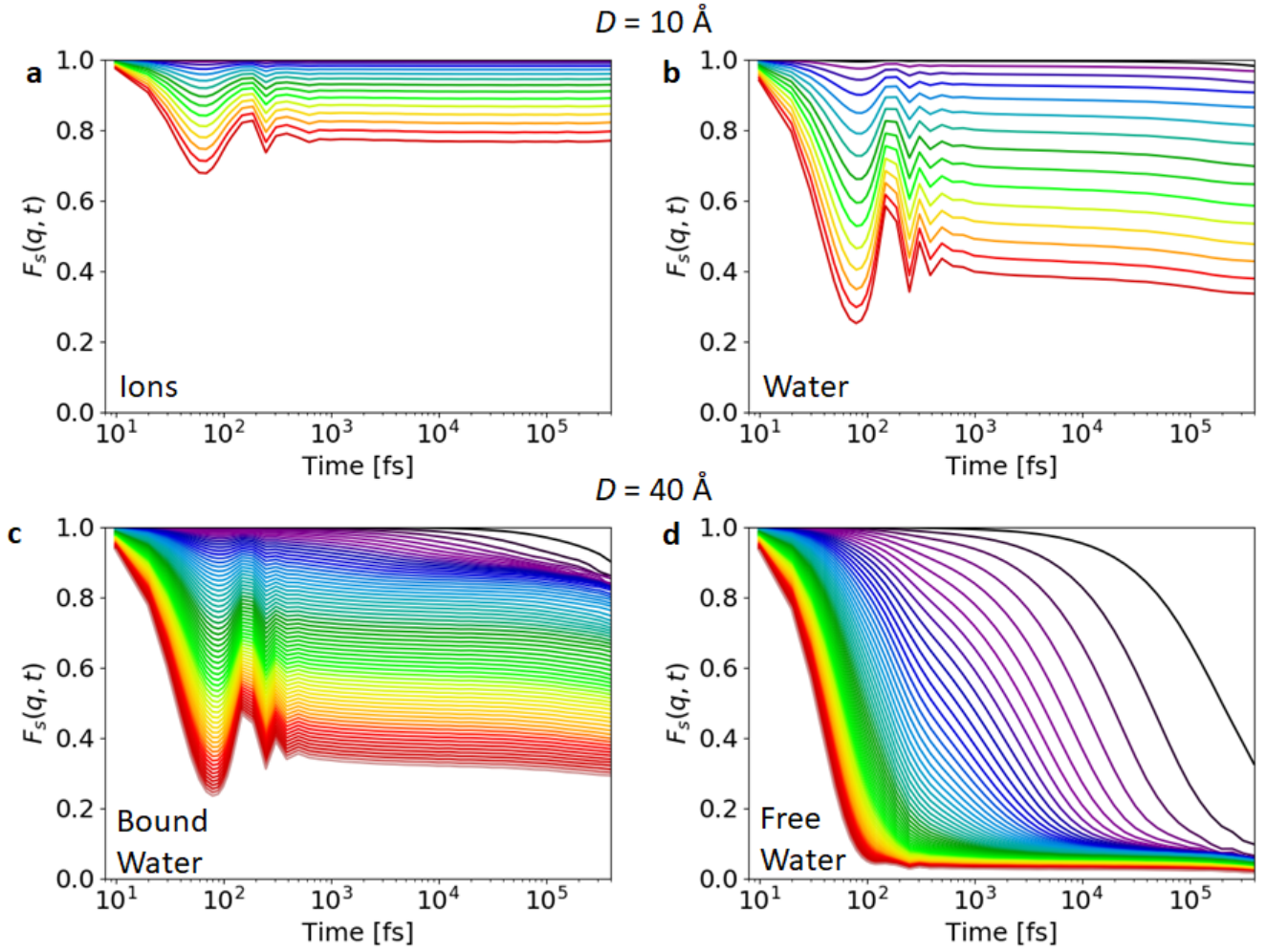
FIG. S2. Self intermediate scattering function at $\sigma = 3e^-/nm^2$ in the z direction (normal to surface plane), for ions or water. Color indicates q from $q = 2\pi/D$ for black to $q = 10\,\text{Å}^{-1}$ for red. (a) Ions in confinement exhibit strong localization near the surfaces. Notably, this does not change when considering larger separations. (b) Same quantity for water. Its dynamics are highly coupled to ion dynamics in confinement. At larger separations, water is split into two populations. The bound water (c), which is close to ions at $t = 0$, follows the ion dynamics, while free water (d) is much more mobile. The dynamical signature of the ions appearing in this bound water demonstrates the stability of ion-water structure and its persistence at larger separations.

experimentally observed increase in physically bound water as a function of hydration time in cement. Changes in the bound water fraction due to C-S-H stoichiometry, including the Ca/Si ratio, can be understood through the effect those changes have on surface charge densities and interlayer distances (i.e. confinement), which in our picture indeed control the ion-water structures. The combined experimental/modeling work of Geng et al [21], for example, shows that the Ca/Si ratio controls the interlayer spacing of C-S-H. As a side note, they also report that decreasing interlayer spacing and an increase in calcium ions is responsible for a rise in the bulk modulus of C-S-H, which is consistent with our results on the cohesion strength.

S2   Strong coupling theory for high surface charge density

At strong confinement, water destructuring heavily alters its electrostatic screening properties. This is due to the presence of solvation shells around Ca^{2+} ions: as shown in Fig. 2 for $\sigma = 3e^-/nm^2$, indeed, ions tend to stick to the walls. We observed that up to a certain distance D between the walls, practically all available water molecules

are used by the system to hydrate Ca^{2+} ions and none is free to move. Figure 4e shows that more than 70% of water molecules are bound to an ion for separations shorter than 10 Å. The hydration of ions results in a huge energy decrease. Albeit associated with a conspicuous entropy reduction, due to positional and orientational localization of water molecules, they are generally favorable in terms of free energy, as we will show in SM section S2.1. This is why, at strong confinement no water molecule is free to move between the two double layers and therefore electrostatic interactions between hydrated ions are not screened. Hydrated, or "dressed" ions (n-mers) behave as effective charged objects, interacting in vacuum: this is referred to in the main paper and in the following as the "locked water" picture.

As a consequence, the relevant Bjerrum length is not $l_B = \frac{\beta e^2}{4\pi\varepsilon_0\varepsilon_r}$ (with $\beta^{-1} = k_B T$), as in bulk water: it is rather close to $l_{B0} = \frac{\beta e^2}{4\pi\varepsilon_0}$, the Bjerrum length in vacuum, that is a factor $\varepsilon_r \simeq 78$ times larger. The effect of this is twofold: 1) the minimum pressure predicted by the contact theorem [64] increases (in absolute value) by a factor 78 from $2\pi l_B\sigma^2$ to around $2\pi l_{B0}\sigma^2$, due to unscreened Coulombic interaction; 2) the coupling parameter Ξ, defined in the Methods, increases from $2\pi q^3 l_B^2\sigma \simeq 75$ to around $2\pi q^3 l_{B0}^2\sigma \simeq 480\,000$ for $\sigma = 3e^-/\mathrm{nm}^2$, thus amply justifying the use of strong coupling theory in the following. These two factors determine a pressure two orders of magnitude higher, in absolute value, than what predicted by primitive models treating water as a dielectric continuum (see SM section S2.2). Our simplification with a drastic decrease of the dielectric permittivity of water, due to confinement, is backed up by a numerical estimate of ε_r based on simulations and the related observations presented in SM section S3.2.

Staggered Wigner crystals have been observed in the literature [65, 66] for coupling higher than $31\,000$. Our large value of the coupling parameter explains then the perfect staggered square crystal observed in Figure 4 for high σ at distance $D = 8$ Å, referred to in the literature [46, 67] as phase III. Due to Lennard-Jones repulsion, the effective distance between the two ionic layers is indeed $D_{\mathrm{eff}} \simeq 3.5$ Å: this corresponds to a dimensionless distance $\eta = D_{\mathrm{eff}}\sqrt{\frac{\sigma}{q}} \simeq 0.43$, at which phase III is expected [46, 67]. In addition, only such a strong coupling can explain the ionic density in Figure 5a, which is strongly peaked close to the walls and vanishes in the whole central region (strong coupling theory does not forbid a uniform ion density, but such a profile appears only at distances D_{eff} ten times smaller).

S2.1 Ion hydration

Energy

We focus here on the mechanism by which water molecules tend to bind to ions and study the energy gain associated to the formation of an n-mer. In simulations, cations tend to lie on parallel planes, at a distance from the closer wall given by the balance between Lennard-Jones interaction and electrostatic attraction. In doing so, they place themselves as close as possible to the walls, so that they expose only a half of their surface for binding with water. This allows us to consider the hydration shell around each ion a hemisphere, around which no more than 6 water molecules can fit. A good estimate of the energy scale at stake is the single dipole-ion interaction energy; in purely electrostatic terms, it can be estimated, in units of $k_B T$, to $-\frac{q\delta l_{B0}}{\sigma_{\mathrm{LJ,eff}}^2} \simeq -70$, where $e\delta = 0.375\,e$Å is the dipole moment of water, l_{B0} is the already mentioned Bjerrum length in vacuum and $\sigma_{\mathrm{LJ,eff}} \simeq 2.5$ Å is the effective distance between the centers of an ion and a water molecule bound to it. The typical dipole-ion interaction energy is much larger, in absolute value, than the typical dipole-dipole interaction energy, which amounts to $-\frac{\delta^2 l_B}{\sigma_{\mathrm{LJ,eff}}^3} \simeq -5$. Adding the Lennard-Jones repulsion, the energy gain per water molecule amounts to $64\,k_B T$, so that the formation energy u_n of an n-mer can be eventually estimated to $-64\,n\,k_B T$ (turquoise line in Figure 4c).

In order to improve this energy estimate, we take into account also dipole-dipole electrostatic and steric interactions. To do so, we consider an ion and n water molecules, fix the ion position at the origin and look for the minimum-energy configuration. We forbid water molecules to assume negative z coordinates in space, i.e. to go beyond the wall. Minimizing through simulated annealing confirms that water prefers to stay close to the ion, with dipoles oriented radially and directed outwards. The so formed n-mers, for $n = 4$, 5 or 6 are depicted in Figure 4c, together with the single-n-mer energies (dark cyan squares). In the following, we refer to water molecules whose dipole moments are parallel to the plane as "coplanar" molecules, and to the water molecule lying on top of the ion, with dipole moment perpendicular to the wall, as the "top" molecule.

Assuming these minimum-energy structures to be the lattice units of an infinite 2D crystal of n-mers, one can eventually compute the energy per n-mer associated to the formation of such crystal, starting from a crystal of ions only. The procedure is non trivial, mainly because of the long range of Coulombic forces: interactions among dipoles and ions were summed discretely up to a sufficiently large distance, from which a continuous approximation was used.
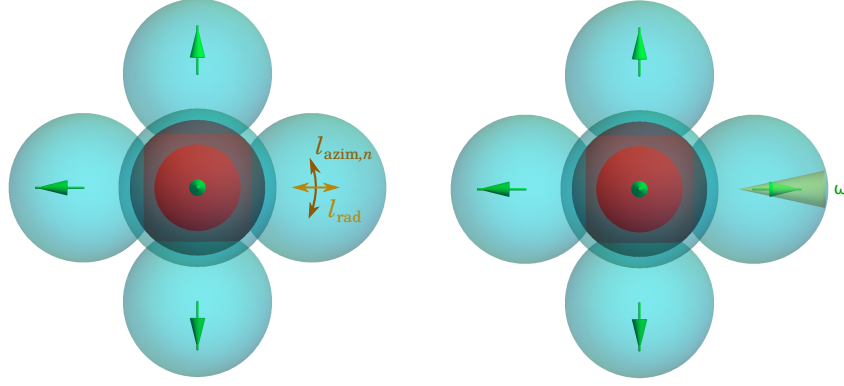
FIG. S3. Top view of two 5-mers (the charged wall lies below the page). On the left, we show the typical fluctuation lengths $l_{\rm rad}$ in the radial direction (closer or further from the ion) and $l_{\rm azim,n}$ in the azimuthal direction (around the ion). On the right, we show the typical solid angle ω spanned by a dipole due to thermal fluctuations. The length of the two arrows and the size of the cone are not to scale.

The resulting energies u_n (green circles in Figure 4c) allow to derive the energy gain in adsorbing a water molecule onto an n-mer to form an $(n+1)$-mer. Notice that u_n/n, i.e. the formation energy of an n-mer per unit dipole, is, in absolute value, more than one order of magnitude higher than thermal energy.

Free energy and n-mer distribution

To confirm the locked-water picture proposed in the previous section, we need to compute the free energy gain $\Delta F_{n\to n+1}$ in adsorbing a water molecule from the bulk on an n-mer, to form an $(n+1)$-mer. We will then check that at strong confinement it is always more favorable for a water molecule to be adsorbed on an ion than to stay in the bulk. The mentioned free energy gain can be calculated as

$$\Delta F_{n\to n+1} = U_{n+1} - U_n - T(S_{n+1} - S_n) - \mu, \tag{S10}$$

where U_n is the average potential energy of water molecules in an n-mer, S_n is their entropy, and μ is the chemical potential of water, i.e. the increase in free energy when a water molecule is moved from the reservoir to the system. What we call here *free energy*, by an abuse of terminology, is properly speaking the *grand-potential*, i.e. the thermo-dynamic potential associated with the grand-canonical ensemble, by which we describe water. Since the situation is grand canonical for water, and canonical for ions (fixed by electro-neutrality), one sometimes uses the terminology of semi-grand-canonical ensemble.

The average energy of an n-mer is $U_n = u_n + \frac{5}{2}n\,k_{\rm B}T$: u_n is for the minimum-energy configuration (green circles in Figure 4c, at our best estimate), plus a contribution per water molecule of $\frac{1}{2}k_{\rm B}T$ for each degree of freedom (3 in real space and 2 in the dipole moment space), assuming that the Hamiltonian can be expanded quadratically around its minimum.

The entropic term S_n can be estimated by considering that a water molecule on an n-mer is confined within a volume $v_n = l_{\rm rad}\,l_{\rm azim,n}^2$ and that its dipole moment is also confined within a solid angle ω (see Fig. S3). $l_{\rm rad}$ is the small radial distance a water molecule can travel further or closer to the ion with a variation in potential energy of the order of $k_{\rm B}T$; it can be estimated within a single water molecule approximation as $l_{\rm rad} \simeq \sqrt{\pi}\,[-\frac{1}{2}U''_{\rm LJ,cd}(\sigma_{\rm LJ,eff}) + 3ql_{\rm B}\delta\sigma_{\rm LJ,eff}^{-4}]^{-1/2} \simeq 0.17\,\text{\AA}$, where $U_{\rm LJ,cd}$ is the charge-dipole (ion-water) Lennard-Jones interaction. In turn, $l_{\rm azim,n}$ is the distance measuring fluctuations of a water molecule along the azimuthal direction around the ion. It can be estimated by fixing positions and dipole moments of all water molecules within the n-mer as in the minimum-energy configuration, except for one probe molecule, which is let free to move on the sphere at constant distance $\sigma_{\rm LJ,eff}$ from the central ion. If our probe is a coplanar molecule we have $l_{\rm azim,4} = 3.1\,\text{\AA}$, $l_{\rm azim,5} = 1.0\,\text{\AA}$ and $l_{\rm azim,6} = 0.30\,\text{\AA}$ (of course, azimuthal confinement grows with n). Lastly, fluctuations in the orientation of the dipole can be estimated by considering that a deviation of the dipole moment of an angle $\delta\theta$ from the equilibrium position produces an increase $\frac{ql_{\rm B}\delta}{\sigma_{\rm LJ,eff}^2}(1 - \cos(\delta\theta))$ in the dimensionless charge-dipole energy, so the solid angle ω corresponding to an energy increase
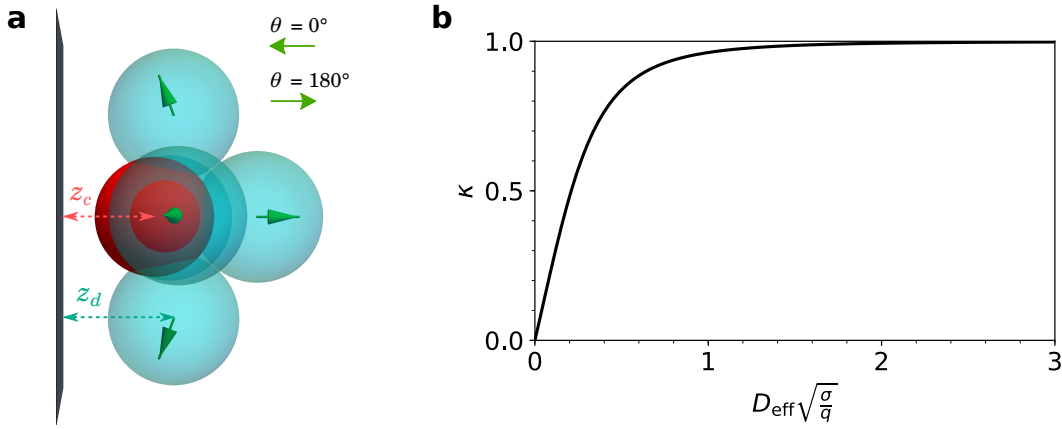
FIG. S4. Minimal energy configuration of an n-mer and the effective field felt by n-mers. (a) Side view of the minimum-energy configuration of 5-mer, interacting with the wall through Lennard-Jones and electrostatic potentials. z_c is the distance of the ion from the wall and z_d is the distance of a coplanar water molecule from the wall. (b) Effective field κ as a function of the dimensionless distance between ion layers $D_{\text{eff}}\sqrt{\sigma/q}$, according to Eq. (S14). This corresponds to the field felt by an ion at contact with the wall, due to the presence of all the surrounding ions. It tends to zero at vanishing distance, when a uniform ion distribution is expected; it tends to unity (i.e. to the single bare wall field) at infinite distance, when correlation with the opposite ion layer is lost.

$k_{\text{B}}T$ is $\omega = \frac{2\pi\sigma_{\text{LJ,eff}}^2}{q l_{\text{B}} \delta} \simeq 0.087$.

Eventually, estimating entropy S_n as $k_{\text{B}} \ln\left[\left(\frac{v_n}{\Lambda^3}\right)^n \omega\right]$, where Λ is the De Broglie thermal wavelength used in μ, Eq. (S10) can be finally rewritten as

$$\Delta F_{n\to n+1} = u_{n+1} - u_n + \frac{5}{2}k_{\text{B}}T - k_{\text{B}}T\ln\left(\frac{v_{n+1}^{n+1}}{\Lambda^3 v_n^n}\omega\right) - \mu\,, \tag{S11}$$

which is independent from Λ, as it should. While $\beta\Delta F_{3\to4}$ and $\beta\Delta F_{4\to5}$ are several tens below zero (< -30 in our estimates), $\beta\Delta F_{5\to6}$ nearly vanishes (-1.1 in our estimate). This suggests that available water molecules must be adsorbed on ions until every ion has 5 water molecules; beyond that point, it becomes in practice equally favourable for water molecules to be adsorbed on a 5-mer and form a 6-mer or to remain in the bulk. This is indeed shown by an analysis of the composition of n-mers as a function of distance D (Figure 4b).

Thermal fluctuations of bound water

An suggested by the relatively high energies involved in the process, the n-mer formation significantly impacts the orientational mobility of water, that is strongly localized close to the ion. At finite temperature, however, water is not completely locked in its ground state configuration and acquires some freedom to move around its equilibrium position. Starting from minimum-energy configurations for n-mers that include interactions with the wall, we analyze the importance of these fluctuations, by computing the probability distribution of the orientation angle of dipoles within the same n-mer. We are thus scrutinizing a fine property, reflecting the effect of temperature on mutual interactions among ions, water molecules and wall altogether.

We fix $n-1$ water molecules to their minimum-energy positions and orientations, and let the remaining one free to move and rotate. Marginalizing numerically with respect to the three spatial degrees of freedom and one of the rotational degrees of freedom, one obtains a probability distribution $p(\theta)$ for the angle θ formed by the dipole moment with respect to the normal of the plane (see Fig. S4a). This can be done using as probe any of the $n-1$ coplanar molecules or the top molecule, for different n.

In Fig. S5 we compare the result of this analysis with simulations using only the dipole interactions for water (as discussed in Methods) for $D = 40\,\text{Å}$. Indeed, the minimum-energy n-mer configuration is computed at $\kappa = 1$ (i.e. $D_{\text{eff}} \gg \sqrt{q/\sigma}$, see Fig. S4b), but results seem to be robust with decreasing D. The theoretical distribution shown is a weighted sum of the distributions computed for coplanar and top dipoles, at $n = 5$ and 6, using the fact that the
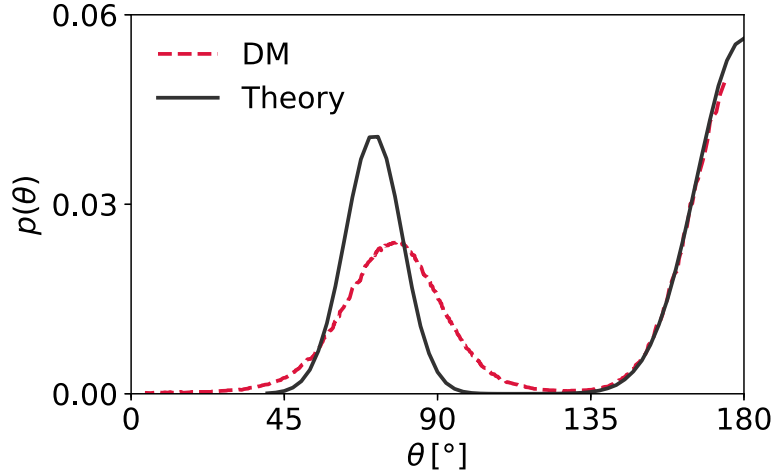
FIG. S5. The probability distribution of the angle between the dipole moment of water in an n-mer and the surface normal at $D = 40\,\text{Å}$. The angle θ is with respect to the nearest surface: $\theta = 0°$ pointing at the surface on which the n-mer resides and $\theta = 180°$ pointing directly away (see Fig. S4a). Contrary to bulk liquid water, the dipole moment is not free and is limited to specific orientations. Due to non-zero temperature, the dipoles fluctuate around these minimum energy positions. The peak at $\theta \simeq 80°$ represents coplanar water molecules, and the one at $\theta = 180°$ top water molecules (see Fig. S4a). At this distance, the former are ~ 4.5 times as many as the former, which would be evidenced by a plot of $p(\theta)\sin\theta$.

fraction of 5-mer and 6-mers is known (Figure 4b). Since this calculation does not allow for cooperative fluctuations away from the ground state, it predicts a distribution that is more sharply peaked, but the result still matches the simulation closely.

Limited resources argument

Supposing all water molecules to bind to Ca^{2+} ions at small D, one can define precise distances D_n at which all ions are bound to exactly n water molecules. At such distances, the following limited-resources equation holds, expressing the fact that the number of water molecules in the pore per unit surface (l.h.s) should equal n times the number of ions per unit surface on both sides (r.h.s.):

$$\rho_{\text{w}}\, D_n = 2\, n\, \frac{\sigma}{q}\,. \tag{S12}$$

Here, ρ_{w} is the total number of water molecules divided by the total simulation volume (D times the surface), so that $\rho_{\text{w}} D$ is the surface density of water. ρ_{w} is a measurable function of D, but it can also be estimated supposing that in the volume effectively available to water (the region at least a Lennard-Jones unit far from walls and ions) the water density is constant (this is true within a 17% error for the considered D range). Anyway, using Eq. (S12) and measured values of ρ_{w}, one obtains $D_3 = 5.9\,\text{Å}$, $D_4 = 6.8\,\text{Å}$ and $D_5 = 7.6\,\text{Å}$. These values are in quantitative agreement with peaks in the observed number of 3-mers, 4-mers and 5-mers as a function of distance (Figure S6).

An interesting observable to look at is the fraction of water molecules bound to ions $f(D)$, shown in Figure 4e. In light of our present discussion, we can provide an analytical description of such curve:

$$f(D) = \begin{cases} 1 & \text{if } D \leq D_5 \\[2mm] \dfrac{10}{10 + \frac{q}{\sigma}\rho_{\text{b}}(D - D_5)} & \text{if } D > D_5 \end{cases}, \tag{S13}$$

where ρ_{b} is the density of bulk water. The factor 10 emerges from the fact that, in a surface q/σ hosting one ion per wall, no more than 10 water molecules (5 on each ion) can be bound. This approximation discards the differences between 5-mers and 6-mers, a valid approximation for our purposes. Also neglected is the presence of a few water molecules, bound to the walls. Nonetheless, this limited resources argument seems to capture all the physical ingredients relevant to explain the numerical curve.
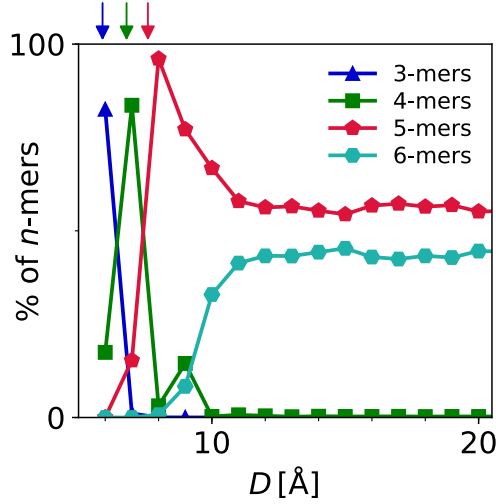
FIG. S6. Equivalent of Figure 4b for simulations with only dipolar water interactions, showing for distances D, percentage of 3-, 4-, 5- and 6-mers observed. Arrows show analytical predictions for D_n, given by Eq. (S13): these correspond to the peaks of the curves shown.

S2.2 Equation of state

Ion densities

In order to compute the density profile and eventually the equation of state, we refined the n-mer minimum-energy configurations discussed in S2.1 by introducing Lennard-Jones and electrostatic interactions with the wall, for the ion and the n water molecules. A numerical minimization of the same kind as the one in SM section S2.1 allows to identify the distances from the wall z_c and z_d at which, respectively, ion (charge) and coplanar water molecules (dipole) prefer to stay. These are better defined by Fig. S4a. The shape of n-mers is qualitatively unchanged, were it not for the fact that 1) ions, charged and slightly smaller, penetrate closer to the wall than water molecules and 2) the dipole moments of coplanar molecules are now slightly tilted toward the wall ($\theta < 90°$ in the Figure). For $n = 5$, $z_c = 2.25$ Å and $z_d = 2.72$ Å and these quantities vary of only a few percent with n. The importance of z_c lies in that it defines the effective distance $D_{\text{eff}} = D - 2z_c$ between the two planes where ions are positioned.

In order to retrieve ion densities, we treat n-mers in their just described minimum-energy configuration as effective charged objects and we use a modified version of the correlation-hole theory described in [14], where we introduce a soft potential $U_{\text{LJ,w}}$ between charges and wall. This potential is the sum of the ion-wall Lennard-Jones potential and of $n - 1$ water-wall Lennard-Jones potentials.

The theory [14] is based on the fact that the effective electric field $\kappa/(\beta q e \mu_0)$ felt by ions lying on one wall is due to the presence of a staggered equal arrangement of ions on the opposite wall (from this perspective, the fields exerted by the two bare walls cancel out exactly). Here, $\mu_0 = (2\pi q l_{\text{B0}} \sigma)^{-1}$ is the Gouy-Chapman length in vacuum, while κ, the dimensionless effective field, is a monotonic function of the distance between the two planes where ions lie. It is useful to recall that κ must be 1 at infinite distance, when ions lying, say, on the left wall feel the presence of the left wall only: since the right wall and its counterions are indeed infinitely far, inter-layer correlation disappears and the right and left half-systems are electroneutral and do not interact. Also, κ must go to 0 at distances $D_{\text{eff}} \ll \sqrt{q/\sigma} \simeq 8$ Å, when ions tend to the uniform distribution along z and are strongly correlated along xy to form a single Wigner crystal [67, 68]. For intermediate distances, the function $\kappa(D_{\text{eff}})$ we use is based on a correlation-hole approach (so-called ch2 in [14]), that has been shown to yield very good results for the liquid ($\Xi \lesssim 31\,000$) and the crystal phase ($\Xi \gtrsim 31\,000$) in the case of point-like ions interacting with hard walls. Within this approximation, the dimensionless effective field, plotted in Figure S4b, is given by

$$\kappa(D_{\text{eff}}) = \frac{D_{\text{eff}}\sqrt{\frac{\sigma}{q}}}{\sqrt{\frac{\sigma}{q}D_{\text{eff}}^2 + \frac{1}{2\pi\left(D_{\text{eff}}\sqrt{\frac{\sigma}{q}}+1\right)}}} . \tag{S14}$$

Now, if we account for Lennard-Jones interactions with the wall, the density ρ of effective charges as a function of distance z between wall and central ion (which is nothing but the ionic density), is given by

$$\frac{\rho(z)}{2\pi l_{\mathrm{B}}\sigma^2} = \mathcal{N}(\mathcal{D})(e^{-\kappa(D_{\mathrm{eff}})\frac{z}{\mu_0} - \beta U_{\mathrm{LJ,w}}(z,D)} + e^{-\kappa(D_{\mathrm{eff}})\frac{D-z}{\mu_0} - \beta U_{\mathrm{LJ,w}}(D-z,D)}),\tag{S15}$$

where $\mathcal{N}(\mathcal{D})$ is a normalization constant, ensuring electroneutrality.

Results of Eq. (S15) are compared with simulations in Figure 5a for $D = 8\,\text{Å}$ and in Figure 5b for $D = 12\,\text{Å}$. Notice that this approximation considers n-mers to be rigid objects and neglects the fact that a $\kappa \neq 1$ can (slightly) modify the n-mer's configuration, namely z_c and z_d. For simplicity, top water molecules (the top dipole in an n-mer) are not considered in $U_{\mathrm{LJ,w}}$. Most importantly, this approximation is not valid at large distances (see SM section S3.2), where free water fills the pore and screens electrostatic interactions – in other words, the Bjerrum and Gouy-Chapman lengths are not constant with D.

Pressure

Once densities are known, one can compute the pressure using the contact theorem, an exact result relating pressure with the ion density at contact with a hard charged wall [64, 69]. We extend this equality in the following way, to account for soft interaction with the wall:

$$P(D) = -\frac{e^2\sigma^2}{2\varepsilon_0} + \int_0^{\frac{D}{2}} F_{\mathrm{LJ,w}}(z)\rho(z)\,\mathrm{d}z\,.\tag{S16}$$

Here, $F_{\mathrm{LJ,w}}(z)$ is the force exerted on both walls by an n-mer in z and corresponds to the derivative of $U_{\mathrm{LJ,w}}(z)$. The sign convention is that positive contributions represent repulsion and negative ones attraction.

The first term in Eq. (S16) represents the minimum pressure attainable due to electrostatic interactions, while the second one, always positive, is due to ions pushing against the walls. The predicted pressure is represented in Fig. 5c and has a minimum at $D_{\min}$ close to $6\,\text{Å}$, corresponding to $P = -6.5\,\text{GPa}$. For smaller distances, the Lennard-Jones repulsion with the wall starts to play a crucial role: pressure increases and eventually becomes positive. This increase must not be mistaken by the pressure increase observed in the hard-wall point-like-ion situation [14], in which case pressure would continue to drop down to a value twice as negative and then increase much more abruptly upon decreasing further the distance. For distances $D > D_{\min}$, the curve is given by:

$$\frac{\beta P(D)}{2\pi l_{\mathrm{B}}\sigma^2} = -1 + \kappa(D_{\mathrm{eff}})\left(\frac{1 + e^{\kappa(D_{\mathrm{eff}})\frac{D_{\mathrm{eff}}}{\mu_0}}}{1 - e^{\kappa(D_{\mathrm{eff}})\frac{D_{\mathrm{eff}}}{\mu_0}}}\right).\tag{S17}$$

This model does not account for solvent layering, which is probably responsible for the non-monotonicity of the curves extracted from numerical simulations. These are plotted in Fig. S7, together with the theoretical prediction from Eq. (S16) and with atomistic simulations of Tobermorite [29]. Atomistic studies that use a more specific C-S-H model have, typically, a higher surface charge density, which should correspond to a higher strength, but this effect could be limited by the presence of surface heterogeneities and other ion types [16]. The good agreement with the atomistic simulations of Ref. [29] is noteworthy, especially remembering that the pressure curve reported there was rationalized by a 7-parameter fit. This is at variance with our theoretical approach, that does not involve any fitting parameter. In Figure 5c of the main text, the theoretical curve is also compared to primitive model simulations run in vacuum. The latter data obey *a fortiori* Eq. (S17), with $D_{\mathrm{eff}} = D - 2z_c$ and $z_c \simeq 2.2\,\text{Å}$, as given by a simple balance between electrostatic attraction to the wall and Lennard-Jones repulsion from it.

Using the saddle point method to estimate $\mathcal{N}(\mathcal{D})$ and the integral in Eq. (S16), it is possible to write the pressure as

$$\beta P(D) = -2\pi l_{\mathrm{B0}}\sigma^2 + \frac{\sigma}{q}\beta F_{\mathrm{LJ,w}}(z_0)\,,\tag{S18}$$

where z_0 is the extremum point of the function appearing to exponential in the Boltmzann factor, that is $\kappa\frac{z}{\mu_0} + \beta U_{\mathrm{LJ,w}}(z)$. Since κ and $F_{\mathrm{LJ,w}}$ depend on D, z_0 does too. The interpretation of this formula is straightforward: since n-mers are concentrated at a distance $\simeq z_0$ from the closest wall ($z_0 = z_c$ at large D), the pressure they exert on the walls is the force $F_{\mathrm{LJ,w}}$ divided by the surface $\frac{q}{\sigma}$ pertaining to each of them. Agreement with the curve calculated from (S16), in black in Fig. S7, is perfect.
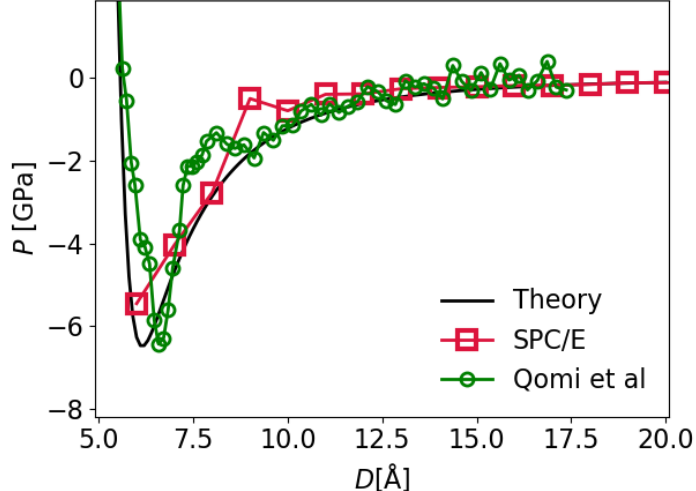
FIG. S7. Pressure P as a function of bare distance between walls D. The theoretical curve, computed from Eq. (S16) and obeying Eq. (S17) for $D > 6\,\text{Å}$ is compared to SPC/E simulations (as in the main text) and to atomistic simulations of a Tobermorite crystal taken from [29]. Pressure data are given in [29] as a function of the distance between the centers of mass of the two solid crystalline walls, also modelled at atomistic level: in order to be presented on this graph, they were shifted to the left by 6.7 Å, which makes the effective distance between ion layers approximately equal to our D_{eff}.

S3   Water properties

S3.1   Water model

Despite significant advances in the past century, water remains a challenging material to model, as evidenced by the plethora of different models developed during that time. In this study, we have opted to use a relatively simple representation of water: the SPC/E model [57]. This model treats water as a rigid molecule, with 3 partial charges and one Lennard-Jones site, which is the minimum degree of complexity needed for hydrogen bonding and a tetrahedral structuring. Nonetheless, it is known that the SPC/E water model effective at capturing the structure and dynamics of bulk water [70].

One weakness of the SPC/E model is that starts to deviate from experimental results in confined or high pressure situations, where the TIP4P/2005 model performs better [58, 71]. Having understood that the phenomena of interest here are related to water-ion structuring and are prevalent when ion-water correlations become dominant on water-water correlations, significant changes in our picture would require dramatic differences in the water model, well beyond the range of the most used ones. Hence we do not expect that our results are qualitatively changed by the more accurate water description of TIP4P/2005. To verify this, we performed additional simulations using the TIP4P/2005 water model, for $\sigma = 3e/\text{nm}^2$ and separations $D = 6$, 8, and 12Å and the same procedure (with due differences in terms of longer simulation times required) for preparation and equilibration of the samples. These simulations showed that the structuring of the ions and the resultant net cohesion between the C-S-H surfaces with the TIP4P/2005 model was very similar to what was obtained with the SPC/E model (Fig. S8).

A final consideration is the effect of polarizability in the water molecule. While one might question whether the interlocked and nearly solid ion-water structure we observe would disappear once polarizability is accounted for, recent studies with polarizable water models for clays have, in fact, demonstrated that the polarizability enhances the slowing down of the water molecule dynamics, indicating that these effects would rather work to confirm our picture [72]. Another study comparing common polarizable and non-polarizable water models confined between MgO surfaces showed that interfacial water structure and orientational patterns were similar, but the polarizable models exhibit more constrained degrees of freedom and longer-ranged water layering—again indicating that polarizability would enhance the effects discussed in our work [73]. To summarize, in the interests of developing a coarse-grained, semi-atomistic approach, the SPC/E water model is overall a reasonable choice.
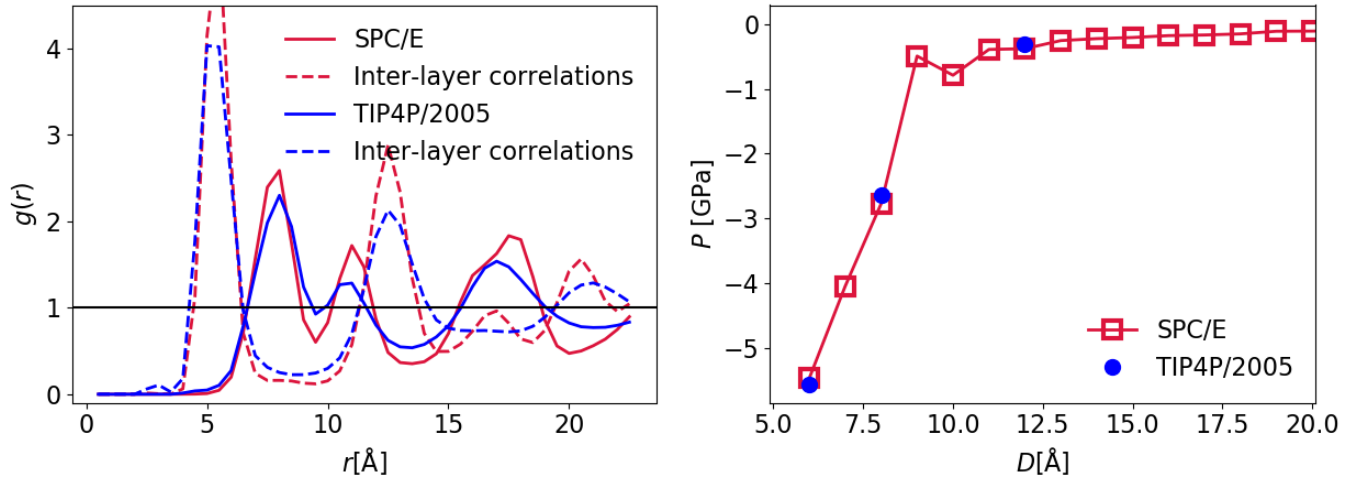
FIG. S8. Comparison between results with SPC/E and TIP4P/2005 models for water at $\sigma = 3e/\text{nm}^2$. The pair correlation $g(r)$ calculated at $D = 8\,\text{Å}$ shows that differences in the water model only slightly alter ion structuring, and the net pressure between the confining surfaces is approximately the same.

S3.2 Dielectric constant

The dielectric response of a material can be quite complex at the atomic level. While the relative dielectric constant ε_r is a macroscopic quantity, it arises from this complex microscopic behavior. Even ignoring how the confinement in our system would change the macroscopic ε_r, trying to use this ε_r for interactions at the nanoscale (as in the PM) has a host of problems. With numerous charges enclosed in a small volume, the polarization of the solvent would depend non-trivially on the arrangement of all the ions and solvent molecules, so taking it to behave the same as in the macroscopic material exposed to an external field is a very strong assumption.

Explicit inclusion of the solvent allows one to directly incorporate this as a microscopic phenomenon. Unfortunately, this is a feature that is actually quite difficult to capture correctly, and many water models that give otherwise similar results produce drastically different values for the dielectric constant [74]. However, while it is difficult to be confident in a precise value, general trends can be informative. In MD simulations, a standard way to compute ε_r is from the total dipole moment, M [75]. ε_r can be related to M through the fluctuation-dissipation theorem. Specifically, $\varepsilon_r = 1 + \chi$, where χ is the electric susceptibility, and the fluctuations in M are related to its dissipation through χ. For an isotropic system, $\langle M \rangle = 0$ and the variance of M is simply $\langle M^2 \rangle$, giving

$$\chi = \frac{1}{\varepsilon_0 V k_\text{B} T} \frac{\langle M_x^2 + M_y^2 + M_z^2 \rangle}{3} . \tag{S19}$$

The behavior of the dielectric constant under confinement is not fully understood. The anisotropy introduced by the slab geometry leads to differing behaviors for ε_{xy} and ε_z. ε_{xy} can be computed in the same way as the bulk calculation except only considering the x and y components of M, while ε_z needs to be reformulated for the very different boundary conditions [76]:

$$\varepsilon_{xy} = 1 + \frac{1}{\varepsilon_0 V k_\text{B} T} \frac{\langle M_x^2 + M_y^2 \rangle}{2} \tag{S20}$$

$$\varepsilon_z^{-1} = 1 - \frac{\langle M_z^2 \rangle}{\varepsilon_0 V k_\text{B} T} . \tag{S21}$$

Using this, we calculate an effective dielectric constant from our simulations (Fig. S9). Though the precise values obtained depend on the model for water, the relative decrease of dielectric constant in confinement is revealing. When all the water is bound to ions, it is highly localized and unable to reorient, leading to a drastically lower dielectric
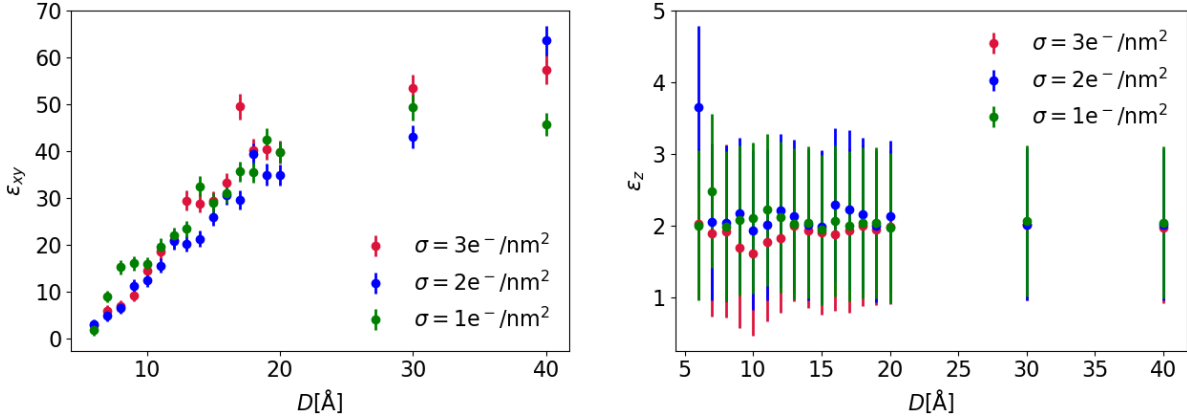
FIG. S9. The transverse (left) and perpendicular (right) relative dielectric constant of water in our simulations, as a function of D. This is computed from the fluctuations of the total water dipole moment. Due to the large coupling between ions and water at small separation, the effective dielectric screening is far lower than the bulk value. The dielectric tensor remains anisotropic even for largest separations considered, which is consistent with experimental measurements of a slow decay in dielectric properties with distance [37].

constant than at larger separations [77]. This lends credence to the locked water picture in which the water is unable to screen electrostatic interactions and helps explain the large increase in net attraction.

The calculation of a dielectric constant is useful to understand, at a qualitative level, how the screening is altered by confinement. However, it is important to note that the effects of water structure and dynamics at a microscopic level cannot be fully captured in a single number in many cases. While it has been proposed that, with Ξ of order a few tens, the results of explicit solvent simulations could be matched by rescaling the bulk dielectric constant in the PM [78], here we find a very different picture, at higher surface charges and for more confined systems, because strong water structuring effects arise. This is seen in the D-dependent, anisotropic dielectric properties and increased cohesion we observe, as well as the hydration-related pressure oscillations (see the pressure spike at $D = 8\,\text{Å}$ and $\sigma = 1e/\text{nm}^2$) which have also been reported in a wide array of studies [41, 79, 80]. What the locked water picture shows is that, in the appropriate limit, a new ground state gains relevance, and water becomes so structured that its effect on the cohesion is minimal—an effect obtained not by partially rescaling the dielectric constant but by assuming that water is not free to screen electrostatic interactions at all.

S4 A bit of history

De caementorum natura, or the invention of C–A–S–H

The invention of modern cement cannot prescind from the discovery of natural cements. These are naturally available sands or mixtures whose mortars feature stronger adhesion than regular lime-based mortars, and, most importantly, hydraulicity: the possibility to set in (sea)-water. While lime mortars seem to have been used by many civilizations millennia BCE in Mesopotamia, Egypt, China and Greece, the first examples of hydraulic natural concrete (sometimes called hydraulic lime) date to 700 BCE. The Nabateans, a bedouin population living between present-day Syria and Jordan, used it to build underground water-proof tanks; their extensive water system (reservoirs, cisterns, aqueduct) allowed them to survive and found settlements in the desert.

The most intense and, at the same time, documented use of natural cement before the modern era is with no doubts to be ascribed to Ancient Romans. Archaeological findings and subsequent scientific analyses [81–83] clearly show that roman harbours had docks and submarine breakwaters built in natural cement. Scientific research has focused on Roman harbours of the west coast of the Italian peninsula, from present-day Southern Tuscany down to the Naples area, but the one of Caesarea, now in Israel, also features huge perfectly preserved concrete blocks that have resisted underwater for two millennia. Archaeologists have conjectured that the naval power Romans had conquered over the Mediterranean by the 2nd century CE was due to a large extent to the fact that their harbours were not only cleverly built, but also built with concrete.

Hydraulicity was not the only property of cement Romans were interested in. They had discovered that concrete was also much stronger than common mortars and started using it for public architecture. The most famous example is undoubtedly the dome of Rome's Pantheon, built by emperor Hadrian in the fist quarter of the 2nd century CE. With its 5 t and 43 m of diameter, it is still the biggest unreinforced concrete dome in the world [84].

What were Romans using to make their concrete? In Roman architect Vitruvius' *De Architectura*, written in the second half of the 1st century BCE, a whole book is devoted to building materials. After describing lime and the proper way to make a mortar out of it, Vitruvius talks about a "powder", that under water suddenly absorbs liquid and quickly hardens, emphasizing heat release. The substance Romans were using, called by Seneca *Puteolanus pulvis* in *Quaestiones Naturales*, goes nowadays by the name *pozzolan*, in Italian *pozzolana*, from the name of the town where it was quarried (Pozzuoli, ancient *Puteoli*, in the Naples region). It is a natural ash of volcanic origin: it works in a very similar manner as modern cement, in that it undergoes a hydration reaction producing C–A–S–H (Calcium Aluminum Silicate Hydrates), a variety of C–S–H where some silicon has been substituted by aluminum.

It is interesting to note that the word cement, and its translation in most European and many non-European modern languages, derives from Latin *caementum* (in turn from *caedere*, to cut), referring to rubble and smashed stone, mostly tuff, that had to be mixed to pozzolana and calcium hydroxide to form concrete.

Romans' astonishment for the fact that "dust, the most insignificant part of the Earth", could "become a single stone, impregnable to the waves, the moment of its immersion, and increase in hardness from day to day" (Pliny the Elder, *Naturalis Historia*) did not lead them to understanding much more about its nature. They only knew, and this was enough for any practical purpose, that it was of volcanic origin and that it must have something to do with high temperature environments ('fire'). This is maybe why the description Vitruvius, in *De Architectura*, makes of the exothermic hydration reactions (echoed by Saint Augustine four centuries later in *De Civitate Dei*) appears so amusingly and surprisingly accurate: "the urgent need of moisture suddenly satiated by water seethes with the latent heat [*calor latens*] in these substances and causes them to gather into a unified mass and gain solidity quickly."

The modern era

After the fall of the Western Roman Empire, cement went back to being practically unknown to architects and builders. To meet cement again in (documented) History, we need to fast-forward to the beginning of the 15th century. Louis XII is king of France and needs to build a bridge over the river Seine in Paris. He asks Venetian architect and clergyman Giovanni Giocondo to develop the project. A man of letters, Giocondo is probably the best living expert of Vitruvius' texts and decides to make use of Neapolitan pozzolan. According to some sources, the then Pont Notre Dasme, inaugurated in 1515 and then completely destroyed and rebuilt through the centuries, presented foundations in natural cement: for the first time after a millennium, pozzolan was being used again for a large-scale work.

Pozzolan is not the only natural earth that produces hydraulic mortars. We know that Dutch builders, at the beginning of the modern era, were using a powder coming from the Eiffel region, between present-day Germany and Belgium. They called it *trass*. Trass (also referred to as terras) had no fortune in commercial exchanges. It would be interesting to understand why, but we will limit ourselves to noticing, as in [85], that its name lacked any appeal: to British it sounded too much like *trash*, and to French it resembled the word *travers*, a flaw.

In the 18th century, people finally started to look for a scientific explanation for the fact that, at first, lime could transform from powder to solid rock, upon addition and consequent evaporation of water. The first attempts were not much closer to reality than the Romans'. Réaumur, Macquer, Becher speak either of some sort of gravity effect or of fire hidden in the stones. Among these fuzzy chemical theories, the documented tips on how to make better mortars flourished: engineer Giovanni Antonio Borgnis suggested to dilute quicklime in wine and add lard or fig juice, while some of his colleagues recommended rather ox blood and urine [86]. In 1783 Antoine-Laurent de Lavoisier finally brought order to this babel of outlandish theories, by discovering oxygen and hydrogen and giving water its chemical formula. This was the birth of modern Chemistry.

If somebody has to be considered the inventor of cement, it should be British engineer John Smeaton (1724-1792) and his baker. The first user of the word "horsepower", before James Watt, and of the expression "civil engineer", as opposed to "military engineer", Smeaton was the designer of a series of bridges, harbours and canals, and, last but not least, of the famous lighthouse of Eddystone. There existed, and still exists, a dangerous stack of rocks, the Eddystone rocks, south of Plymouth, in the English Channel. Throughout history, many ships had sunk there during tempests and since the end of the 17th century people had tried to build a lighthouse to warn sailors of their presence. The first two attempts were taken down due to the strength of storms and to fires. When Smeaton was asked to build the third lighthouse, he started experimenting new kinds of mortars that could resist storms. One day he prepared a mixture of limestone and ordinary clay and took it to the bakery asking that it be baked in the oven

at high temperature. When the result of his experiment came back, he noticed that the substance he had produced could harden in water and solidify to form a rock of the same kind as portlandite (from where the modern name of Portland cement). Using this substance, together with pozzolan coming from Italy, that for some reason he seemed to still trust unconditionally, he built a new lighthouse between 1756 and 1759, also known as the Smeaton tower. Had it not been for the underlying rocks, that were eroded by water, the lighthouse would still stand firmly where it was. It was actually removed in 1877.

Smeaton's studies were published right before his death and were probably read by James Parker, who filed a patent of dubious originality in 1796 and started the first business producing "Roman cement" – this was its commercial name – together with John Bazley White. Meanwhile in France, Louis Vicat was also studying hydraulicity: probably also influenced by Smeaton's work he published in 1818 the result of his *Recherches expérimentales sur les chaux de contruction, les bétons et les mortiers ordinaires*, that was translated and read all over Europe. Also a civil engineer, he completed in 1824 the first bridge ever built with artificial cement, in Souillac, Southern France.

John Apsdin's patent, filed in 1824, and similar to Maurice Saint-Léger's, filed some years before with Vicat's contribution, marked the birth of another cement-producing company. Most importantly, it gave the opportunity to Apsdin's son, William, to apply his rebellious temperament to experimenting new techniques for making cement. One day he overcooked a sample, to the point that it had vitrified. Before throwing it away, he had the idea to pulverize what appeared as a block of burnt rock: he then noticed that, upon hydration, this magic powder formed a much stronger concrete than what he was used to. He had just invented clinker and modern Portland cement. Aspdin's recipe was then improved by his competitor Isaac Charles Johnson in the 1850's and, besides minor changes, is the one still in use in cement factories nowadays.

The fortune of cement in the following two centuries is there for all to see. Starting with the tunnel under river Thames, completed by Marc Brunel in 1843, cement has gained a leading position in infrastructure, public and residential building, and, with a bit more difficulty, in design and architecture. This was a long process that would not have been possible without the mechanization and centralization of the productive chain, initially motivated by entrepreneurs' necessity to get rid of the corporations of stone cutters. It was the 19th century and the second industrial revolution had just begun.

REFERENCES AND NOTES

1. International Energy Agency (IEA) for the Global Alliance for Buildings and Construction (GlobalABC), "Global Alliance for Buildings and Construction 2018 Global Status Report," (Technical Report, UN Environment Programme, 2018.

2. G. Habert, S. A. Miller, V. M. John, J. L. Provis, A. Favier, A. Horvath, K. L. Scrivener, Environmental impacts and decarbonization strategies in the cement and concrete industries. *Nat. Rev. Earth Environ.* **1**, 559–573 (2020).

3. A. J. Allen, J. J. Thomas, H. M. Jennings, Composition and density of nanoscale calcium-silicate-hydrate in cement. *Nat. Mater.* **6**, 311–316 (2007).

4. M. J. Abdolhosseini Qomi, K. J. Krakowiak, M. Bauchy, K. L. Stewart, R. Shahsavari, D. Jagannathan, D. B. Brommer, A. Baronnet, M. J. Buehler, S. Yip, F. J. Ulm, K. J. Van Vliet, R. J. Pellenq, Combinatorial molecular optimization of cement hydrates. *Nat. Commun.* **5**, 4960 (2014).

5. K. Ioannidou, K. J. Krakowiak, M. Bauchy, C. G. Hoover, E. Masoero, S. Yip, F.-J. Ulm, P. Levitz, R. J.-M. Pellenq, E. Del Gado, Mesoscale texture of cement hydrates. *Proc. Natl. Acad. Sci.* **113**, 2029–2034 (2016).

6. R. J.-M. Pellenq, H. van Damme, Why does concrete set?: The nature of cohesion forces in hardened cement-based materials. *MRS Bullet.* **29**, 319–323 (2004).

7. C. Plassard, E. Lesniewska, I. Pochard, A. Nonat, Nanoscale experimental investigation of particle interactions at the origin of the cohesion of cement, *Langmuir* 21, 7263–7270 (2005).

8. A. Gmira, M. Zabat, R. J. Pellenq, H. Van Damme, Microscopic physical basis of the poromechanical behavior of cement-based materials. *Mat. Struct.* **37**, 3–14 (2004).

9. J. Israelachvili, *Intermolecular and Surface Forces* (Academic Press, ed. 3, 2011).

10. Y. S. Jho, R. Brewster, S. A. Safran, P. A. Pincus, Long-range interaction between heterogeneously charged membranes, *Langmuir* **27**, 4439–4446, 2011.

11. W. M. Gelbart, R. F. Bruinsma, P. A. Pincus, V. A. Parsegian, Dna-inspired electrostatics. *Phys. Today* 53, 38–44 (2000).

12. Y. Levin, Electrostatic correlations: From plasma to biology. *Rep. Prog. Phys.* **65**, 1577–1632 2002).

13. A. G. Moreira, R. R. Netz, Binding of similarly charged plates with counterions only. *Phys. Rev. Lett.* **87**, 78301 (2001).

14. L. Samaj, M. Trulsson, E. Trizac, Strong-coupling theory of counterions between symmetrically charged walls: From crystal to fluid phases. *Soft Matter* **14**, 4040–4052 (2018).

15. B. Carrier, "Influence of water on the short-term and long-term mechanical properties of swelling clays: Experiments on self-supporting films and molecular simulations," thesis, Universite Paris-Est (2014).

16. S. Masoumi, S. Zare, H. Valipour, M. J. Abdolhosseini Qomi, Effective interactions between calcium-silicate-hydrate nanolayers. *J. Phys. Chem. C* **123**, 4755–4766 (2019).

17. B. Jönsson, H. Wennerström, A. Nonat, B. Cabane, Onset of cohesion in cement paste. *Langmuir* **20**, 6702–6709 (2004).

18. R. J. Pellenq, N. Lequeux, H. van Damme, Engineering the bonding scheme in C–S–H: The iono-covalent framework. *Cem. Concr. Res.* **38**, 159–174 (2008).

19. M. Vandamme, F.-J. Ulm, Nanogranular origin of concrete creep. *Proc. Natl. Acad. Sci.* **106**, 10552–10557 (2009).

20. R. K. Mishra, A. K. Mohamed, D. Geissbühler, H. Manzano, T. Jamil, R. Shahsavari, A. G. Kalinichev, S. Galmarini, L. Tao, H. Heinz, R. Pellenq, A. C. van Duin, S. C. Parker, R. J. Flatt, P. Bowen, *cemff*: A force field database for cementitious materials including validations, applications and opportunities. *Cem. Concr. Res.* **102**, 68–89 (2017).

21. G. Geng, R. J. Myers, M. J. A. Qomi, P. J. Monteiro, Densification of the interlayer spacing governs the nanomechanical properties of calcium-silicate-hydrate. *Sci. Rep.* **7**, 10986 (2017).

22. J. W. Bullard, H. M. Jennings, R. A. Livingston, A. Nonat, G. W. Scherer, J. S. Schweitzer, K. L. Scrivener, J. J. Thomas, Mechanisms of cement hydration. *Cem. Concr. Res.* **41**, 1208–1223 (2011).

23. C. Meral, C. J. Benmore, P. J. Monteiro, The study of disorder and nanocrystallinity in C–S–H, supplementary cementitious materials and geopolymers using pair distribution function analysis. *Cem. Concr. Res.* **41**, 696–710 (2011).

24. C. E. White, L. L. Daemen, M. Hartl, K. Page, Intrinsic differences in atomic ordering of calcium (alumino)silicate hydrates in conventional and alkali-activated cements. *Cem. Concr. Res.* **67**, 66–73 (2015).

25. J. J. Thomas, S. A. FitzGerald, D. A. Neumann, R. A. Livingston, State of water in hydrating tricalcium silicate and portland cement pastes as measured by quasi-elastic neutron scattering, *J. Am. Ceram. Soc.* **84**, 1811–1816 (2001).

26. H. N. Bordallo, L. P. Aldridge, A. Desmedt, Water dynamics in hardened ordinary portland cement paste or concrete: From quasielastic neutron scattering. *J. Phys. Chem. B* **110**, 17966–17976 (2006).

27. A. J. Bohris, U. Goerke, P. J. McDonald, M. Mulheron, B. Newling, B. Le Page, A broad line NMR and MRI study of water and water transport in portland cement pastes, *Magn. Reson. Imaging* **16**, 455–461 (1998)

28. E. Fratini, A. Faraone, F. Ridi, S. H. Chen, P. Baglioni, Hydration water dynamics in tricalcium silicate pastes by time-resolved incoherent elastic neutron scattering. *J. Phys. Chem. C* **117**, 7358–7364 (2013).

29. S. Masoumi, H. Valipour, M. J. Abdolhosseini Qomi, Intermolecular forces between nanolayers of crystalline calcium-silicate-hydrates in aqueous medium. *J. Phys. Chem. C* **121**, 5565–5572 (2017).

30. I. G. Richardson, G. W. Groves, Microstructure and microanalysis of hardened ordinary Portland cement pastes. *J. Mater. Sci.* **28**, 265–277 (1993).

31. B. Lothenbach, A. Nonat, Calcium silicate hydrates: Solid and liquid phase composition. *Cem. Concr. Res.* **78**, 57–70 (2015).

32. W. S. Chiang, E. Fratini, P. Baglioni, D. Liu, S. H. Chen, Microstructure determination of calcium-silicate-hydrate globules by small-angle neutron scattering. *J. Phys. Chem. C* **116**, 5055–5061 (2012).

33. C. Labbez, I. Pochard, B. Jönsson, A. Nonat, C-S-H/solution interface: Experimental and Monte Carlo studies, *Cem. Concr. Res.* **41**, 161–168 (2011).

34. L. B. Skinner, S. R. Chae, C. J. Benmore, H. R. Wenk, P. J. M. Monteiro, Nanostructure of calcium silicate hydrates in cements. *Phys. Rev. Lett.* **104**, 195502 (2010).

35. A. Schlaich, E. W. Knapp, R. R. Netz, Water dielectric effects in planar confinement. *Phys. Rev. Lett.* **117**, 048001 (2016).

36. N. Giovambattista, P. J. Rossky, P. G. Debenedetti, Phase transitions induced by nanoconfinement in liquid water. *Phys. Rev. Lett.* **102**, 050603 (2009).

37. L. Fumagalli, A. Esfandiar, R. Fabregas, S. Hu, P. Ares, A. Janardanan, Q. Yang, B. Radha, T. Taniguchi, K. Watanabe, G. Gomila, K. S. Novoselov, A. K. Geim, Anomalously low dielectric constant of confined water. *Science* **360**, 1339–1342 (2018).

38. S. Koneshan, J. C. Rasaiah, R. M. Lynden-Bell, S. H. Lee, Solvent structure, dynamics, and ion mobility in aqueous solutions at 25 C. *J. Phys. Chem. B* **102**, 4193–4204 (1998).

39. T. Megyes, T. Grósz, T. Radnai, I. Bakó, G. Pálinkás, Solvation of calcium ion in polar solvents: An x-ray diffraction and ab initio study. *J. Phys. Chem. A* **108**, 7261–7271 (2004).

40. D. W. Smith, Ionic hydration enthalpies. *J. Chem. Educ.* **54**, 540–542 (1977).

41. P. M. Claesson, P. Herder, P. Stenius, J. C. Eriksson, R. M. Pashley, An ESCA and AES study of ion-exchange on the basal plane of mica. *J. Colloid Interface Sci.* **109**, 31–39 (1986).

42. X. Shen, I. C. Bourg, Molecular dynamics simulations of the colloidal interaction between smectite clay nanoparticles in liquid water. *J. Colloid Interface Sci.* **584**, 610–621 (2021).

43. K. Ioannidou, R. J.-M. Pellenq, E. Del Gado, Controlling local packing and growth in calcium-silicate-hydrate gels. *Soft Matter* **10**, 1121–1133 (2014).

44. K. Ioannidou, M. Kanduč, L. Li, D. Frenkel, J. Dobnikar, E. Del Gado, The crucial effect of early-stage gelation on the mechanical properties of cement hydrates. *Nat. Commun.* **7**, 12106 (2016).

45. A. Goyal, K. Ioannidou, C. Tiede, P. Levitz, R. J.-M. Pellenq, E. Del Gado, Heterogeneous surface growth and gelation of cement hydrates. *J. Phys. Chem. C* **124**, 15500–15510 (2020).

46. L. Šamaj, E. Trizac, Ground state of classical bilayer Wigner crystals. *EPL* **98**, 36004 (2012).

47. K. L. Scrivener, P. Juilland, P. J. Monteiro, Advances in understanding hydration of Portland cement. *Cem. Concr. Res.* **78**, 38–56 (2015).

48. S. Bishnoi, K. L. Scrivener, Studying nucleation and growth kinetics of alite hydration using μic. *Cem. Concr. Res.* **39**, 849–860 (2009).

49. P. D. Tennis, H. M. Jennings, A model for two types of calcium silicate hydrate in the microstructure of Portland cement pastes. *Cem. Concr. Res.* **30**, 855–863 (2000).

50. K. Ioannidou, E. Del Gado, F.-J. Ulm, R. J.-M. Pellenq, Inhomogeneity in cement hydrates: Linking local packing to local pressure *J. Nanomech. Micromech.* **7**, 04017003 (2017).

51. M. Abuhaikal, K. Ioannidou, T. Petersen, R. J. Pellenq, F. J. Ulm, Le Châtelier's conjecture: Measurement of colloidal eigenstresses in chemically reactive materials. *J. Mech. Phys. Solids* **112**, 334–344 (2018).

52. T. Zhou, K. Ioannidou, F.-J. Ulm, M. Z. Bazant, R. J.-M. Pellenq, Multiscale poromechanics of wet cement paste, *Proc. Natl. Acad. Sci.* **116**, 10652–10657 (2019).

53. A. Aili, M. Vandamme, J. M. Torrenti, B. Masson, Is long-term autogenous shrinkage a creep phenomenon induced by capillary effects due to self-desiccation? *Cem. Concr. Res.* **108**, 186–200 (2018).

54. H. Van Damme, in *Colloidal Chemo-Mechanics of Cement Hydrates and Smectite Clays: Cohesion vs. Swelling* (Taylor & Francis, 2006), pp. 1411–1426.

55. C. Merlet, B. Rotenberg, P. A. Madden, P. L. Taberna, P. Simon, Y. Gogotsi, M. Salanne, On the molecular origin of supercapacitance in nanoporous carbon electrodes. *Nat. Mater.* **11**, 306–310 (2012).

56. S. Plimpton, Fast parallel algorithms for short-range molecular dynamics *J. Comput. Phys.* **117**, 1–19 (1995).

57. H. J. C. Berendsen, J. R. Grigera, T. P. Straatsma, The missing term in effective pair potentials. *J. Phys. Chem.* **91**, 6269–6271 (1987).

58. J. L. Abascal, C. Vega, A general purpose model for the condensed phases of water: TIP4P/2005. *J. Chem. Phys.* **123**, 234505 (2005).

59. R. T. Cygan, J.-J. Liang, A. G. Kalinichev, Molecular models of hydroxide, oxyhydroxide, and clay phases and the development of a general force field. *J. Phys. Chem. B.* **108**, 1255–1266 (2004).

60. M. P. Allen and D. J. Tildesley, *Computer Simulation of Liquids* (Oxford Univ. Press, 1987).

61. I.-C. Yeh, M. L. Berkowitz, Ewald summation for systems with slab geometry. *J. Chem. Phys.* **111**, 3155–3162 (1999).

62. J.-P. Hansen, I. McDonald, *Theory of Simple Liquids* (Academic Press, ed. 3, 2006).

63. Y. Zhang, M. Lagi, F. Ridi, E. Fratini, P. Baglioni, E. Mamontov, S. H. Chen, Observation of dynamic crossover and dynamic heterogeneity in hydration water confined in aged cement paste. *J. Phys. Condens. Matter* **20**, 502101 (2008).

64. D. Andelman, Introduction to electrostatics in soft and biological matter, in *Soft Condensed Matter Physics in Molecular and Cell Biology*, W. C. K. Poon, D. Andelman, Eds. (CRC Press, 2006), pp. 97–122.

65. A. G. Moreira, R. R. Netz, Simulations of counterions at charged plates. *Eur. Phys. J. E* **8**, 33–58 (2002).

66. H. Boroudjerdi, Y.-W. Kim, A. Naji, R. R. Netz, X. Schlagberger, A. Serr, Statics and dynamics of strongly charged soft matter. *Phys. Rep.* **416**, 129–199 (2005).

67. G. Goldoni, F. M. Peeters, Stability, dynamical properties, and melting of a classical bilayer wigner crystal. *Phys. Rev. B* 53, 4591–4603 (1996).

68. E. Trizac, L. Samaj, Like-charge colloidal attraction: A simple argument, in *Proceedings of the International School of Physics Enrico Fermi*, C. Bechinger, F. Sciortino, P. Ziherl, Eds. (IOS, Amsterdam, 2012), vol. 184, pp. 61–73.

69. D. Henderson, L. Blum, J. Lebowitz, An exact formula for the contact value of the density profile of a system of charged hard spheres near a charged wall. *J. Electroanal. Chem.* **102**, 315–319 (1979).

70. P. Mark, L. Nilsson, Structure and dynamics of the TIP3P, SPC, and SPC/E water models at 298 K. *Chem. A Eur. J.* **105**, 9954–9960 (2001).

71. J. Dix, L. Lue, P. Carbone, Why different water models predict different structures under 2D confinement. *J. Comput. Chem.* **39**, 2051–2059 (2018).

72. S. Le Crom, C. Tournassat, J.-C. Robinet, V. Marry, Influence of polarizability on the prediction of the electrical double layer structure in a clay mesopore: A molecular dynamics study. *J. Phys. Chem. C* **124**, 6221–6232 (2020).

73. G. Kamath, S. A. Deshmukh, S. K. Sankaranarayanan, Comparison of select polarizable and non-polarizable water models in predicting solvation dynamics of water confined between MgO slabs. *J. Phys. Condens. Matter* **25**, 305003 (2013).

74. M. Sprik, Hydrogen bonding and the static dielectric constant in liquid water. *J. Chem. Phys.* **95**, 6762–6769 (1991).

75. C. G. Gray, Y. S. Sainger, C. G. Joslin, P. T. Cummings, S. Goldman, Computer simulation of dipolar fluids. Dependence of the dielectric constant on system size: A comparative study of Ewald sum and reaction field approaches. *J. Chem. Phys.* **85**, 1502 (1986).

76. V. A. Froltsov, S. H. L. Klapp, Dielectric response of polar liquids in narrow slit pores. *J. Chem. Phys.* **126**, 114703 (2007).

77. A. Schlaich, A. P. dos Santos, R. R. Netz, Simulations of nanoseparated charged surfaces reveal charge-induced water reorientation and nonadditivity of hydration and mean-field electrostatic repulsion *Langmuir* **35**, 551–560 (2019).

78. L. Pegado, B. Jönsson, H. Wennerström, Ion-ion correlation attraction in a molecular solvent. *J. Chem. Phys.* **129**, 184503 (2008).

79. E. Schneck, F. Sedlmeier, R. R. Netz, Hydration repulsion between biomembranes results from an interplay of dehydration and depolarization. *Proc. Natl. Acad. Sci.* **109**, 14405–14409 (2012).

80. H. Chen, J. R. Cox, H. Ow, R. Shi, A. Z. Panagiotopoulos, Hydration repulsion between carbohydrate surfaces mediated by temperature and specific ions. *Sci. Rep.* **6**, 28553 (2016).

81. M. D. Jackson, J. Moon, E. Gotti, R. Taylor, S. R. Chae, M. Kunz, A. H. Emwas, C. Meral, P. Guttmann, P. Levitz, H. R. Wenk, P. J. Monteiro, Material and elastic properties of Al-tobermorite in ancient roman seawater concrete, *J. Am. Ceram. Soc.* **96**, 2598–2606 (2013).

82. M. D. Jackson, S. R. Mulcahy, H. Chen, Y. Li, Q. Li, P. Cappelletti, H.-R. Wenk, Phillipsite and Al-tobermorite mineral cements produced through low-temperature water-rock reactions in Roman marine concrete. *Am. Mineral.* **102**, 1435–1450 (2017).

83. J. P. Oleson, C. Brandon, S. M. Cramer, R. Cucitore, E. Gotti, R. L. Hohlfelder, The ROMACONS project: A contribution to the historical and engineering analysis of hydraulic concrete in Roman maritime structures. *Int. J. Nautical Archaeol.* **33**, 199–229 (2004).

84. D. Moore, *The Roman Pantheon: The Triumph of Concrete* (MARC/CCEOP, University of Guam Station, 2010).

85. R. Courland, *Concrete planet: The strange and Fascinating story of the World's Most Common Man-Made Material* (Prometheus Books, 2011).

86. C. Simonnet, *Le béton: Histoire d'un Matériau: Économie, Technique, Architecture* (Parenthèses, 2005).